

Machine Learning Exchange Fields for Ab-initio Spin Dynamics

Yuqiang Gao,^{1,2} Menno Bokdam,² and Paul J. Kelly²

¹*School of Physics and Electronic Information, Anhui Province Key Laboratory for Control and Applications of Optoelectronic Information Materials, Anhui Normal University, Wuhu 241000, PR China*

²*University of Twente, Faculty of Science and Technology and MESA+ Institute for Nanotechnology, P.O. Box 217, 7500 AE Enschede, The Netherlands*

(Dated: 19 March 2024)

We add the magnetic degrees of freedom to the widely used Gaussian Approximation Potential of machine learning (ML) and present a model that describes the potential energy surface of a crystal based on the atomic coordinates as well as their noncollinear magnetic moments. Assuming an adiabatic approximation for the spin directions and magnitudes, the ML model depends solely on spin coordinates and orientation, resulting in computational efficiency and enabling *ab initio* spin dynamics. Leveraging rotational symmetries of magnetic interactions, the ML model can incorporate various magnetic interactions, expanding into two-body, three-body terms, etc., following the spirit of cluster expansion. For simplicity, we implement the ML model with a two-body form for the exchange interaction. Comparing total energies and local fields predicted by the model for noncollinear spin arrangements with explicit results of constrained noncollinear density functional calculations for bcc Fe yields excellent results, within 1 meV/spin for the total energy. Further optimization, including three-body and other terms, is expected to encompass diverse magnetic interactions and enhance the model's accuracy. This will extend the model's applicability to a wide range of materials and facilitate the machine learning *ab initio* spin dynamics.

PACS numbers: 75.70.Ak, 73.22.-f, 75.30.Hx, 75.50.Pp

I. INTRODUCTION

At finite temperatures, the magnetic moments of magnetic materials vary with time in magnitude and direction influencing the potential energy surface (PES) that describes the motion of the ions. The purpose of this publication is to extend to itinerant magnetic materials recently developed methods for performing first-principles (FP) molecular dynamics (MD) simulations. This requires taking the spin degrees of freedom into consideration by extending the concept of “machine-learning force fields” (ML-FF) to “machine-learning exchange fields” (ML-EF) and will ultimately entail performing coupled ionic and spin dynamics. We begin with a brief summary of the recent relevant progress in first-principles (or *ab-initio*) molecular dynamics, FP-MD (or AIMD).

In the Car-Parrinello *ab-initio* molecular dynamics (AIMD) scheme [1], the interactions between the atoms comprising molecules and solids are described in terms of full quantum mechanical (QM) solutions for the constituent electrons. AIMD founders ultimately on the need to describe the electron and ion dynamics on the same short time scale necessary to keep the electrons in their ground state [2]. For metals with no gap between occupied and unoccupied states, it turns out to be more efficient to combine long molecular-dynamics (MD) time steps for the ions with full self-consistent field (SCF) solutions of the Kohn-Sham equations of Density Functional Theory (DFT) [3, 4] for the electrons. Every such step yields the total electronic energy that plays the role of a potential energy for the ionic motion, the forces acting on all the atoms, and the stress tensor [5]. The re-

sulting Born-Oppenheimer MD (BO-MD) procedure is limited by the DFT calculation to time scales of tens of picoseconds (ps) for thousands of atoms [2] (hundreds of ps for hundreds of atoms [6]). For comparison, typical optical vibration frequencies are in the range $10^{12} - 10^{13}$ Hertz. In these simulations, many of the computationally expensive DFT calculations are unnecessary because at temperatures at which bonds are only seldom broken, much of the simulation time is spent repeatedly exploring a tiny portion of the $3N$ dimensional coordinate space. The effectiveness of modelling a huge diversity of systems using periodic boundary conditions is such that N is determined by the size of the unit cell required to model the system of interest and far smaller than the $N \approx 10^{23}$ atoms composing a typical solid. Typically N should be of order 10^3 to avoid artifacts of the artificial periodicity but such large systems are usually prohibitively expensive. For metallic or nonpolar materials, the range of the interatomic force constants is quite limited, to of order ~ 30 atoms (the long range electrostatic interactions in polar solids can be taken care of classically without significantly increasing the computational cost). The challenge is to find an efficient parameterization of the DFT BO potential energy surface (PES) in this enormously reduced but still very large coordinate space.

Behler and Parrinello decomposed the total potential energy U_{tot} of a system of interacting atoms into a sum of local atomic contributions U_i

$$U_{\text{tot}} = \sum_{i=1}^N U_i(\{\mathbf{r}_j\} - \mathbf{r}_i), \quad (1)$$

and replaced the Cartesian coordinates $\{\mathbf{r}_j\}$ on which U_i

depends with coordinates (“descriptors”) that reflect the translational, rotational, reflectional and permutational symmetry of atom i , so-called “atom-centered symmetry functions” (ACSF) [2]. This innovation received a great deal of attention and has stimulated much subsequent activity. Observing that the PES is a relatively smooth function of the coordinates on which it depends and using the same atomic decomposition of the potential energy as [2], Bartok *et al.* introduced the density $\rho_i(\mathbf{r})$ at position \mathbf{r} of the atomic neighbours of each atom i

$$\rho_i(\mathbf{r}) = \sum_j^{r_{ij} < r_{\text{cut}}} f_{\text{cut}}(r_{ij}) \delta(\mathbf{r} - \mathbf{r}_{ij}), \quad (2)$$

in terms of δ functions at each atomic position. Here the index j runs over the neighbors of atom i at \mathbf{r}_i within some radius r_{cut} , $\mathbf{r}_{ij} = \mathbf{r}_j - \mathbf{r}_i$ and $r = |\mathbf{r}|$. The smooth cutoff function $f_{\text{cut}}(r)$ removes information about the structure beyond r_{cut} and a commonly made choice is $f_{\text{cut}}(r) = [1 + \cos(\pi r/r_{\text{cut}})]/2$ [2, 7, 8]. $\rho(\mathbf{r})$ should characterize an atomic environment uniquely. Bartok *et al.* described the radial dependence in terms of an angle, expanded ρ in “hyperspherical” harmonics and reduced the determination of the BO-PES to interpolating atomic energies U_i in this space. To do this, they introduced a non-parametric method called “Gaussian process regression” and called the resulting PES the “Gaussian Approximation Potential” (GAP) [7]. Because of the delta functions used to describe the atomic positions, the expression (2) for $\rho_i(\mathbf{r})$ is not smooth and this leads to difficulties characterizing the similarity of different atomic environments. Replacing the δ functions with Gaussians led to a smooth measure of similarity that was termed “Smooth Overlap of Atomic Positions” (SOAP) [9].

In spite of the great reduction in the size of the coordinate space made possible by the approximations outlined above, a huge number of calculations is still needed to determine the BO-PES to perform AIMD, even for simple materials. A considerable improvement was described by Jinnouchi *et al.* whereby new DFT calculations are only performed for an uncharted volume of coordinate space when the MD simulation explores that volume of coordinate space, so-called “on-the-fly machine learning (ML)”. The criterion for deciding to perform a new DFT calculation is in essence based upon the distance of the new region of coordinate space from regions already explored and the estimate of the error in the potential energy and forces based upon a Bayesian regression analysis that lends itself to full automation [8, 10].

In the “machine-learning force-field (ML-FF)” approach just sketched, the electronic degrees of freedom have been effectively integrated out and Newton’s equations of motion are solved for the ionic degrees of freedom using an effective force field that is determined quantum mechanically and interpolated in the coordinate space. As a result a much longer time step appropriate to the ionic dynamics can be used. For magnetic materials we will develop an analogous procedure whereby the spatial

distribution of the spin density will be integrated out to yield atomic moments and effective (exchange) field which enter Landau-Lifshitz-like (LL) equations that will be solved to describe the dynamics of atomic magnetic moments.

The LL equations describe the time variation of a magnetization $\mathbf{M}(\mathbf{r}, t)$ in an effective magnetic field $\mathbf{H}_{\text{eff}}(t)$ as

$$\frac{\partial \mathbf{M}(\mathbf{r}, t)}{\partial t} = -\gamma \mathbf{M}(\mathbf{r}, t) \times \mathbf{H}_{\text{eff}}(\mathbf{r}, t) \quad (3)$$

where γ is the gyromagnetic ratio $g\mu_B/\hbar$, $\mu_B = e\hbar/2m_e$ is the Bohr magneton and $g \sim 2$ and

$$\mathbf{H}_{\text{eff}}(\mathbf{r}, t) = \frac{\partial F[\mathbf{M}]}{\partial \mathbf{M}} \quad (4)$$

[11, 12]. The effective field can usually be decomposed into contributions from applied, dipolar demagnetization, crystal-anisotropy and exchange fields. In this manuscript we will be focussing on bulk itinerant ferromagnets like Fe so that the applied, demagnetization and anisotropy fields can be neglected by comparison with the exchange field. In (3) and (4), $\mathbf{M}(\mathbf{r}, t)$ and $\mathbf{H}_{\text{eff}}(\mathbf{r}, t)$ are vector fields and solution of the LL equation forms the subject of “micromagnetism” [11]. Since we are interested in a first-principles description of magnetization dynamics, we will replace the continuum vector fields with discrete atomic quantities as in “atomistic spin dynamics (ASD)” [13, 14]. We will present a novel descriptor for noncollinear spins which takes into account both the spin orientation and atomic coordinates within the GAP framework [7, 15]. Our ML model effectively captures the DFT total energies and effective magnetic field of non-collinear spin structures at different temperatures. This achievement demonstrates the broad applicability and accuracy of our approach with the simplified ML model.

The paper is organized as follows. Section II introduces the methodology used to build the descriptor for the non-collinear spin structures. Section II A presents the power spectrum of the SOAP descriptor. In Section II B, we expand the spin orientation vector in spherical harmonics and introduce the SOAP analogue for spins, the “smooth overlap of spin orientation” (SOSO). In Sections II C and II D, we derive the descriptor and kernels for magnetic exchange and dipole-dipole interactions, respectively. In Section III, the performance of the ML model is tested. Because the energy of magnetic dipole-dipole, magnetic anisotropy (and other) interactions are so small compared to the exchange interaction in cubic Fe, we only consider the exchange interaction here. In Section III A, we conduct constrained self-consistent first principle calculations for non-collinear spin systems to train and test the ML model. In Section III B, the ML model is tested on a Heisenberg Hamiltonian with varying magnitude of the magnetic moment and atomic positions. We compare our model to similar recent work in Section IV. The adiabatic approximation for the spin simplifies the ML model, thereby manifesting a notable

enhancement in computational efficiency and enabling the machine learning *ab initio* spin dynamics, as summarized in Section V.

II. METHODOLOGY

The main challenge in developing an effective ML model for magnetic materials is to efficiently represent the local environment seen by a spin \mathbf{s} characterized by its magnitude s , its orientation $\hat{\mathbf{e}} = \mathbf{s}/s$ and its position \mathbf{r} . At finite temperatures it is subject to longitudinal and transverse fluctuations [16] that lead to a huge phase space for the non-collinear spin system. The typical interatomic exchange parameters J_{ij} are small (e.g. < 30 meV for Fe, Co, Ni [17]) compared to the characteristic electronic energies such as intraatomic exchange, interatomic hopping, etc. Thus the spin orientation corresponds to the slow degrees of freedom (\sim ps) while the evolution of the spin magnitudes is determined by the change of the electronic wave functions (fast degrees of freedom \sim fs). By analogy with the Born-Oppenheimer approximation in molecular dynamics [18], the adiabatic approximation between the rotation of the spin orientation and fluctuations of the magnitude of the spin can be made because of their different time scales [19]. Therefore, the ML model can be constructed solely based on the spin orientation and its location (which is just the corresponding atomic position). This will greatly contract the phase space for the non-collinear system and improve the efficiency of the ML model. Variation of the spin magnitude can be included at the expense of expanding the dimension of the descriptor space to include s explicitly.

A key to the success of the ML-FFs was the incorporation of the translational and rotational invariance in the formulation of the atomic interactions. To design the magnetic PES, mapping the local spin configurations onto a symmetry-adapted descriptor can reduce the phase space of noncollinear spin systems enormously. The target property should be invariant under translational, rotational, reflectional and permutational symmetry operations. These symmetries can be found from a magnetic Hamiltonian [20] such as

$$H = -J \sum_{i \neq j} \mathbf{s}_i \cdot \mathbf{s}_j - P \sum_{i \neq j} \frac{3(\mathbf{s}_i \cdot \mathbf{r}_{ij})(\mathbf{s}_j \cdot \mathbf{r}_{ij}) - \mathbf{s}_i \cdot \mathbf{s}_j}{|\mathbf{r}_{ij}|^3} - K \sum_i (\mathbf{s}_i \cdot \mathbf{e}_K)^2 - \sum_{i \neq j} D_{ij} \cdot [\mathbf{s}_i \times \mathbf{s}_j] \quad (5)$$

where on the right-hand side the four most important magnetic interactions in magnetic materials are listed. From left to right, these are the interatomic exchange, magnetic dipole-dipole, magnetocrystalline anisotropy and Dzyaloshinskii–Moriya (DMI) interactions. \mathbf{s}_i and \mathbf{s}_j represent the local spin on sites i and j , respectively; \mathbf{e}_K is the direction of the anisotropy axis. By making use of the rotational symmetry of the magnetic interactions,

TABLE I. Calculated magnetic energies of bulk bcc Fe, hcp Co and fcc Ni (meV/atom). MAE: magnetocrystalline anisotropy (μ eV/atom), Co from Ref. [21], Fe and Ni from Ref. [22]; DMI: Dzyaloshinskii-Moriya interaction (meV) in thin film or multilayer interface [23–25].

	Fe	Co	Ni
$E_{\text{FM}} - E_{\text{NM}}$	561	208	58
$E_{\text{FM}} - E_{\text{AFM}}$	459	203	56
E_{MA}	1.4	65	2.7
DMI	0.15	0.18	0.12

the phase space can be contracted. In this way the ML PES would accurately capture isotropic magnetic interactions. The energy of magnetic dipole-dipole interaction is normally of order 0.1 meV per atom and is comparable to the size of the DMI interaction, Table I. For the anisotropic part that depends on the crystal geometry, including magnetocrystalline anisotropy (that is considerably smaller in energy scale, of the order of μ eV/atom compared to isotropic exchange interactions that is of the order of 100 meV/atom) as indicated in Table I, an additional correction should be incorporated. However, in this work, we will focus on the isotropic magnetic interaction, in particular the exchange interactions that dominate the total energy of the spin systems.

In the spirit of the cluster expansion [26], the total energy can be expanded in a sum of n -body (cluster) interaction terms ($n = 1, 2, \dots, \infty$). For example, the simple Coulomb interaction was expanded in two-body and three-body terms in the ML force field in [8]. Although there have been discussions about its completeness, it would appear that the accuracy of present ML force fields considering up to three-body terms is already sufficiently high; it has been argued that decomposing the total energy into a sum of atom-centered contributions mitigates the influence of fundamental deficiencies of this approach [27]. Therefore, in this work on magnetic interactions, we will only consider two and three-body terms. Depending on the rotational symmetry of magnetic interactions, the spin and coordinates vectors are coupled in different way as shown in Table II. The exchange interaction depends on the two spin vectors, \mathbf{s}_i and \mathbf{s}_j , along with their separation, r_{ij} . For an isotropic exchange interaction, the Hamiltonian must remain invariant when both \mathbf{s}_i and \mathbf{s}_j are rotated by the same angle. The three-body term, involving higher-order exchange interactions, depends on the three spin vectors, \mathbf{s}_i , \mathbf{s}_j and \mathbf{s}_k as well as the separations d_{ij} and d_{ik} from \mathbf{s}_i , where the Hamiltonian maintains its invariance under simultaneous rotations of \mathbf{s}_i , \mathbf{s}_j and \mathbf{s}_k . In contrast, the classical magnetic dipole-dipole interaction in (5) depends on \mathbf{s}_i , \mathbf{s}_j , and their relative position vector, \mathbf{r}_{ij} . The corresponding two-body term retains rotational invariance when \mathbf{s}_i , \mathbf{s}_j , and \mathbf{r}_{ij} are rotated by the same angle. In this work, we will develop descriptors for exchange interactions and dipole-dipole interactions with rotational symmetries extending up to

TABLE II. The coupled vectors that are rotationally invariant for different descriptors. “2b” and “3b” denote two-body and three-body, respectively.

	\mathbf{r}_{ij}	\mathbf{r}_{ik}	$\hat{\mathbf{s}}_i$	$\hat{\mathbf{s}}_j$	$\hat{\mathbf{s}}_k$
Exchange-2b	-	-	coupled	coupled	-
Exchange-3b	-	-	coupled	coupled	coupled
Dipole-2b	coupled	-	coupled	coupled	-
Dipole-3b	coupled	coupled	coupled	coupled	coupled

three-body terms.

In contrast to conventional machine learning force fields, which primarily address the Coulomb interactions based on the local atomic environments, machine learning force fields for magnetic systems require an expansion of the phase space to include not only atomic positions but also spin orientations. To compare the similarity of two spin systems, we will extend the SOAP method, originally designed to distinguish two local structures with the smooth overlap of atomic positions, to calculate the similarity of two local spin structures with what we will call “Smooth Overlap of Spin Orientations (SOSO)”. Considering that magnetic interactions are influenced by atomic separations, the SOSO framework will include the smooth overlap of atomic positions as well.

A. Smooth overlap of atomic positions (SOAP)

In the GAP framework, the potential energy U of a structure with N_a atoms is approximated as a sum of local energies U_i as

$$U = \sum_{i=1}^{N_a} U_i. \quad (6)$$

Each local energy U_i is assumed to be fully determined by the local environment of atom i described by the smooth atomic density distribution

$$\rho_i(\mathbf{r}) = \sum_{j=1}^{N_a} f_{\text{cut}}(\mathbf{r}_{ij}) g(\mathbf{r} - \mathbf{r}_{ij}), \quad (7)$$

in which $g(r)$ is the normalized Gaussian function

$$g(\mathbf{r} - \mathbf{r}_{ij}) = \frac{1}{(\sqrt{2}\sigma_{\text{atom}}\pi)^3} \exp\left(-\frac{(\mathbf{r} - \mathbf{r}_{ij})^2}{2\sigma_{\text{atom}}^2}\right). \quad (8)$$

By expanding it in plane waves [28], the Gaussian function can be expressed in spherical harmonics

$$\rho_i(\mathbf{r}) = \sum_{j=1}^{N_a} f_{\text{cut}}(\mathbf{r}_{ij}) \frac{1}{(\sqrt{2}\sigma_{\text{atom}}\pi)^3} \exp\left(-\frac{r^2 + r_{ij}^2}{2\sigma_{\text{atom}}^2}\right) \quad (9)$$

$$4\pi \sum_{l=0}^{L_{\text{max}}} \sum_{m=-l}^{m=l} j_l\left(\frac{rr_{ij}}{\sigma_{\text{atom}}}\right) Y_{lm}^*(\hat{\mathbf{r}}_{ij}) Y_{lm}(\hat{\mathbf{r}}).$$

where we use spherical coordinates $\mathbf{r} = (r, \theta, \phi)$ and the notation $\hat{\mathbf{r}} = (\theta, \phi)$ for the unit vector. j_l is the spherical Bessel function. On expanding the radial part in a set of radial basis functions $\chi(r)$ [29], the atomic density can be rewritten as

$$\rho_i(\mathbf{r}) = \sum_{n=1}^{N_R^i} \sum_{l=1}^{L_{\text{max}}} \sum_{m=-l}^l c_{nlm}^i \chi_{nl}(r) Y_{lm}(\hat{\mathbf{r}}), \quad (10)$$

where the coefficient c_{nlm}^i has the form

$$c_{nlm}^i = \sum_{j=1}^{N_a} h_{nl}(r_{ij}) Y_{lm}^*(\hat{\mathbf{r}}_{ij}), \quad (11)$$

with which the rotationally invariant three-body term [8] that is equivalent to the power spectrum [9]

$$p_{nn'l}^i = \sum_m c_{nlm}^i c_{n'l m}^{i*}. \quad (12)$$

can be constructed. The three-body term decomposes the local atomic environment of atom i into triplets involving atoms i , j and k represented by the power spectrum. Then the similarity kernel of two different atomic configurations can be calculated by the overlap of these sets in two different configurations as in (13).

In (11), the radial coefficient c_{nlm}^i is expressed as a sum of spherical harmonics describing the positions of atoms j with respect to the central atom i . Multiplication of two c_{nlm}^i generates all possible combinations of r_{ij} and r_{ik} , which corresponds to the three-body term. The sum over m for the coupling of two spherical harmonics with the same angular momentum number l in (12) indicates the rotational invariance according to the addition theorem of spherical harmonics whereby two angular momenta are coupled to zero. The kernel that measures the similarity of two local structures \mathbf{X} and \mathbf{X}' can be indicated from the smooth overlap of the atomic position (SOAP) of two structures and written as

$$K(\mathbf{X}, \mathbf{X}') = \sum_{nn'l} p_{nn'l} \rho_{nn'l}^i. \quad (13)$$

where each vector \mathbf{X}_i collects all coefficients c_n^i and $p_{nn'l}^i$ for a specific local configuration $\rho_i(\mathbf{r})$.

B. Smooth overlap of spin orientation (SOSO)

By analogy with SOAP, we use a Gaussian distribution function to describe the spin orientation $\hat{\mathbf{e}}$ and the overlap between two different spin structures. Because of the “adiabatic approximation” for spin according to which the spin orientation varies slowly in time whereas its magnitude varies more rapidly [30], we only consider the direction of the spin on atom i expressed in terms of the unit vector $\hat{\mathbf{e}}_i$

$$g(\hat{\mathbf{e}} - \hat{\mathbf{e}}_i) \sim \exp\left(-\frac{(\hat{\mathbf{e}} - \hat{\mathbf{e}}_i)^2}{2\sigma^2}\right) \quad (14)$$

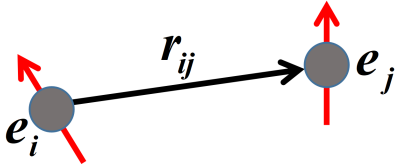


FIG. 1. Schematic of exchange interaction between two neighbouring spins. \mathbf{e}_i , \mathbf{e}_j represent the unit direction vectors of spins i (\mathbf{s}_i) and j (\mathbf{s}_j), respectively. \mathbf{r}_{ij} denotes the relative position vector between two spins.

where σ determines the width of the Gaussian. To obtain the normalization factor, we integrate the Gaussian function over the surface of the unit sphere with $\hat{\mathbf{e}}_i = (0, 0, 1)$

$$\int g(\hat{\mathbf{e}} - \hat{\mathbf{e}}_i) d\hat{\mathbf{e}} \sim \int_0^\pi \exp\left(-\frac{1}{\sigma^2}\right) \exp\left(\frac{\cos\theta}{\sigma^2}\right) d\theta \quad (15)$$

$$= \exp\left(-\frac{1}{\sigma^2}\right) \pi I_0\left(\frac{1}{\sigma^2}\right),$$

where $I_0(x)$ is the modified Bessel function of the first kind. The normalised Gaussian function can be rewritten as

$$g(\hat{\mathbf{e}} - \hat{\mathbf{e}}_i) = \frac{\exp(\frac{1}{\sigma^2})}{\pi I_0(\frac{1}{\sigma^2})} \exp\left(-\frac{(\hat{\mathbf{e}} - \hat{\mathbf{e}}_i)^2}{2\sigma^2}\right), \quad (16)$$

which represents the spin orientation distribution (SOD) on the unit sphere at site i . Expanding in spherical harmonics, it can be rewritten as

$$g(\hat{\mathbf{e}} - \hat{\mathbf{e}}_i) = \frac{\exp(\frac{1}{\sigma^2})}{\pi I_0(\frac{1}{\sigma^2})} 4\pi \exp\left(-\frac{1}{\sigma^2}\right) \sum_{l=0}^{L_{\max}} \sum_{m=-l}^l j_l\left(\frac{1}{\sigma^2}\right) Y_{lm}^*(\hat{\mathbf{e}}_i) Y_{lm}(\hat{\mathbf{e}}) \quad (17)$$

$$= \frac{4}{I_0\left(\frac{1}{\sigma^2}\right)} \sum_{l=0}^{L_{\max}} \sum_{m=-l}^l j_l\left(\frac{1}{\sigma^2}\right) Y_{lm}^*(\hat{\mathbf{e}}_i) Y_{lm}(\hat{\mathbf{e}}).$$

$$S(\hat{R}) = \iiint r^2 dr d\hat{\mathbf{e}}_1 d\hat{\mathbf{e}}_2 \rho(r, \hat{\mathbf{e}}_1, \hat{\mathbf{e}}_2) \rho'(r, \hat{R}\hat{\mathbf{e}}_1, \hat{R}\hat{\mathbf{e}}_2) = \sum_{\substack{m_1, m_2 \\ m'_1, m'_2 \\ l_1, l_2}} C_{l_1 l_2 m_1 m_2}^* C'_{l_1 l_2 m'_1 m'_2} D_{m_1 m'_1}^{(l_1)}(R) D_{m_2 m'_2}^{(l_2)}(R) \quad (20)$$

where we use the relation

$$Y_{lm}^*(\hat{R}\hat{\mathbf{e}}) = \sum_{m'=-l}^l Y_{lm'}^*(\hat{\mathbf{e}}) D_{m'm}^{(l)}(\hat{R}) \quad (21)$$

and $D_{m'm}^{(l)}(\hat{R})$ are the Wigner rotation matrices for the rotation \hat{R} [9, 31].

C. Descriptor for interatomic exchange interaction

First we consider the descriptor for the dominant interatomic exchange interaction in magnetic materials. It can be constructed by substituting the SODs for sites i and j in (7). Introducing the spin degree of freedom into (7), which adds the SODs defined in Eq.(17) for spins at sites i and j .

$$\rho_i(\mathbf{r}, \hat{\mathbf{e}}_1, \hat{\mathbf{e}}_2) = \sum_{j=1}^{N_a} f_{\text{cut}}(r_{ij}) g(\mathbf{r} - \mathbf{r}_{ij}) g(\hat{\mathbf{e}}_1 - \hat{\mathbf{e}}_i) g(\hat{\mathbf{e}}_2 - \hat{\mathbf{e}}_j), \quad (18)$$

in which $\hat{\mathbf{e}}_1$ and $\hat{\mathbf{e}}_2$ are independent unit spin variable. Because of the short range of the exchange interaction, a cutoff function $f_{\text{cut}}(r_{ij})$ will be used to only consider the spins within the cutoff distance.

In the classical Heisenberg Hamiltonian (5), the interatomic exchange energy $E_{\text{ex}} = \sum_{i \neq j} J_{ij}(R) \mathbf{s}_i \cdot \mathbf{s}_j$. Because $J_{ij}(R)$ is distance dependent and E_{ex} is invariant under simultaneous rotations of \mathbf{s}_i and \mathbf{s}_j , the spin density distribution descriptor can be obtained by integrating the descriptor in (18) over the unit sphere $\hat{\mathbf{r}}$ because the exchange interaction between spins depends on their separation r , not their orientation $\hat{\mathbf{r}}$.

$$\rho_i(r, \mathbf{e}_1, \mathbf{e}_2) = \int d\hat{\mathbf{r}} \sum_{j=1}^{N_a} f_{\text{cut}}(r_{ij}) g(\mathbf{r} - \mathbf{r}_{ij}) g(\mathbf{e}_1 - \mathbf{e}_i) g(\mathbf{e}_2 - \mathbf{e}_j). \quad (19)$$

Consider the rotational invariance of $\mathbf{s}_i \cdot \mathbf{s}_j$. Under an arbitrary rotation \hat{R} the overlap S of two local spin structures becomes

The similarity kernel can be derived as

$$\begin{aligned}
K(\rho, \rho') &= \int S(\widehat{R})dR = \sum_{\substack{m_1, m_2 \\ m'_1, m'_2 \\ l_1, l_2}} C_{l_1 l_2 m_1 m_2}^* C'_{l_1 l_2 m'_1 m'_2} \int D_{m_1 m'_1}^{(l_1)}(\widehat{R}) D_{m_2 m'_2}^{(l_2)}(\widehat{R}) d\widehat{R} \\
&= \sum_{\substack{m_1, m_2 \\ m'_1, m'_2 \\ l_1, l_2}} C_{l_1 l_2 m_1 m_2}^* C'_{l_1 l_2 m'_1 m'_2} (-1)^{m_1 - m'_1} \int D_{-m_1, -m'_1}^{(l_1)}(\widehat{R})^* D_{m_2 m'_2}^{(l_2)}(\widehat{R}) d\widehat{R} \\
&= \sum_{m_1, m'_1, l} \frac{8\pi^2 (-1)^{m_1 + m'_1}}{2l + 1} C_{lm_1, -m_1}^* C'_{lm'_1, -m'_1}
\end{aligned} \tag{22}$$

where $d\widehat{R}$ indicates integration over all possible rotations [9] and

$$Y_{lm}^*(r) = (-1)^m Y_{l, -m}(r). \tag{23}$$

Here the kernel does not integrate the square of $S(R)$ as in the case of SOAP. Because exchange interaction is in principle a two-body interaction, the kernel defined here only includes the two-body term of the exchange interaction. For three-body or higher order terms, it can be constructed from the descriptor defined in (A1) (see Appendix A).

Now we have given the full expression for the kernel of two-body term of exchange interaction. The exchange interaction does not depend on the direction of \mathbf{r}_{ij} , so only the scalar radial distribution part r_{ij} left. For computational efficiency, we expend the radial part of spin density into orthogonal radial basis functions $\chi_{nl}(r)$. Then the radial distribution density of spin $\rho_i(r)$ can be rewritten as

$$\rho_i(r) = \frac{1}{\sqrt{4\pi}} \sum_{n=1}^{N_R} C_{n00}^i \chi_{nl}(r). \tag{24}$$

Therefore, by summing the coefficients in (22) over m , we can get

$$\begin{aligned}
C_{nl}^i &= \sum_j^{N_a} C_{n00}^i \left(\frac{4}{I_0(\sigma^{-2})} \right)^2 \sum_{m=-l}^l j_l^2(\sigma^{-2}) Y_{lm}^*(\hat{\mathbf{e}}_i) Y_{lm}(\hat{\mathbf{e}}_j) \\
&= \sum_j^{N_a} C_{n00}^i \left(\frac{4}{I_0(\sigma^{-2})} \right)^2 j_l^2(\sigma^{-2}) \frac{2l+1}{4\pi} P_l(\cos \theta_{ij})
\end{aligned} \tag{25}$$

Adding the prefactor $\sqrt{\frac{8\pi^2}{2l+1}}$,

$$C_{nl}^i = \sum_j^{N_a} C_{n00}^i \left(\frac{4}{I_0(\frac{1}{\sigma^2})} \right)^2 j_l^2\left(\frac{1}{\sigma^2}\right) \sqrt{\frac{2l+1}{8\pi}} P_l(\cos \theta_{ij}). \tag{26}$$

The similarity kernel can be rewritten as

$$K(\rho_i, \rho'_i) = \sum_{n,l} C_{nl}^{i*} C_{nl}^i. \tag{27}$$

D. Descriptor for magnetic dipole-dipole like interaction

Here, we also give the descriptor for magnetic dipole-dipole like interactions that maintain the rotational symmetry of $\mathbf{s}_i, \mathbf{s}_j$, and \mathbf{r}_{ij} .

$$\rho_i(\mathbf{r}, \hat{\mathbf{e}}_1, \hat{\mathbf{e}}_2) = \sum_{j=1}^{N_a} f_{cut}(r_{ij}) g(\mathbf{r} - \mathbf{r}_{ij}) g(\hat{\mathbf{e}}_1 - \hat{\mathbf{e}}_i) g(\hat{\mathbf{e}}_2 - \hat{\mathbf{e}}_j). \tag{28}$$

The overlap of two local spin structures

$$\begin{aligned}
S(\widehat{R}) &= \iiint r^2 d\widehat{\mathbf{r}} d\hat{\mathbf{e}}_1 d\hat{\mathbf{e}}_2 \rho(\mathbf{r}, \hat{\mathbf{e}}_1, \hat{\mathbf{e}}_2) \rho'(\widehat{R}\mathbf{r}, \widehat{R}\hat{\mathbf{e}}_1, \widehat{R}\hat{\mathbf{e}}_2) \\
&= \sum_{\substack{m, m_1, m_2 \\ m', m'_1, m'_2 \\ l, l_1, l_2}} C_{ll_1 l_2; mm_1 m_2}^* C'_{ll_1 l_2; m' m'_1 m'_2} \\
&\quad D_{mm'}^l(\hat{\mathbf{e}}) D_{m_1 m'_1}^{l_1}(\hat{\mathbf{e}}) D_{m_2 m'_2}^{l_2}(\hat{\mathbf{e}}).
\end{aligned} \tag{29}$$

To get the similarity kernel, we need to transform the Wigner D-matrix to be complex conjugate of another D-matrix by

$$D_{mm'}^l(R) = (-1)^{m-m'} D_{-m, -m'}^l(R)^*. \tag{30}$$

Then, the integrate of three D-matrix can be expressed as

$$\begin{aligned}
&\int D_{mm'}^l(R)^* D_{m_1 m'_1}^{l_1}(R) D_{m_2 m'_2}^{l_2}(R) dR \\
&= \frac{8\pi^2}{2l+1} \langle lm | l_1 m_1; l_2 m_2 \rangle \times \langle lm' | l_1 m'_1; l_2 m'_2 \rangle,
\end{aligned} \tag{31}$$

in which the angle brackets are Clebsch–Gordan coefficients.

Finally, the similarity kernel can be written as

$$\begin{aligned}
K(\rho, \rho') &= \int S(R) dR = \sum_{\substack{m, m_1, m_2 \\ m', m'_1, m'_2 \\ l, l_1, l_2}} C_{ll_1 l_2 m m_1 m_2}^* C'_{ll_1 l_2 m' m'_1 m'_2} \int D_{mm'}^l(R) D_{m_1 m'_1}^{l_1}(R) D_{m_2 m'_2}^{l_2}(R) dR \\
&= \sum_{\substack{m, m_1, m_2 \\ m', m'_1, m'_2 \\ l, l_1, l_2}} C_{ll_1 l_2 m m_1 m_2}^* C'_{ll_1 l_2 m' m'_1 m'_2} (-1)^{m-m'} \int D_{-m, -m'}^l(R)^* D_{m_1 m'_1}^{l_1}(R) D_{m_2 m'_2}^{l_2}(R) dR \\
&= \sum_{\substack{m, m_1, m_2 \\ m', m'_1, m'_2 \\ l, l_1, l_2}} C_{ll_1 l_2 m m_1 m_2}^* C'_{ll_1 l_2 m' m'_1 m'_2} \frac{8\pi^2 (-1)^{m+m'}}{2l+1} \langle l, -m | l_1 m_1; l_2 m_2 \rangle \times \langle l, -m' | l_1 m'_1; l_2 m'_2 \rangle.
\end{aligned} \tag{32}$$

The Clebsch–Gordan coefficients will only be nonzero when

$$|l_1 - l_2| < l < l_1 + l_2 \tag{33a}$$

$$m_1 + m_2 = -m \tag{33b}$$

$$m'_1 + m'_2 = -m' \tag{33c}$$

Therefore, the coefficient in (32) can be rewritten as radial part $C_{nlm_1+m_2}^i$ and spin vector part $C_{l_1 l_2, m_1 m_2}^i$

$$C_{nlm_1+m_2}^i = \sum_{j=1}^{N_a} h_{nl}(r_{ij}) Y_{lm_1+m_2}(\hat{\mathbf{r}}_{ij}) \tag{34}$$

$$\begin{aligned}
C_{l_1 l_2, m_1 m_2}^i &= \sum_j \left(\frac{4}{I_0 \left(\frac{1}{\sigma^2} \right)} \right)^2 j_{l_1} \left(\frac{1}{\sigma^2} \right) j_{l_2} \left(\frac{1}{\sigma^2} \right) \\
&\quad Y_{l_1 m_1}^*(\hat{\mathbf{e}}_j) Y_{l_2 m_2}^*(\hat{\mathbf{e}}_k) \\
&\quad \sqrt{\frac{8\pi^2}{2l+1}} \langle l, m_1 + m_2 | l_1 m_1; l_2 m_2 \rangle.
\end{aligned} \tag{35}$$

Now we have got the similarity kernel for two-body term of magnetic dipole-dipole interaction. For the three-body term, we can not use the traditional power spectrum, because the spin direction at spin i is shared by the spin j and k . Here, we can define the three body spin distribution as

$$\begin{aligned}
\rho_i(r_1, r_2, e_1, e_2, e_3) &= \sum_{j \neq k}^{N_a} f_{cut}(\mathbf{r}_{ij}) g(\mathbf{r}_1 - \mathbf{r}_{ij}) g(\mathbf{r}_2 - \mathbf{r}_{ik}) \\
&\quad g(\mathbf{e}_1 - \mathbf{e}_i) g(\mathbf{e}_2 - \mathbf{e}_j) g(\mathbf{e}_3 - \mathbf{e}_k).
\end{aligned} \tag{36}$$

III. TRAINING AND TESTING

Because the interatomic exchange interaction constitutes the primary contribution to the total energy in ferromagnets as indicated in Table I, a GAP-SOSO ML

model is constructed analogous to the GAP-SOAP framework, incorporating a two-body term of the exchange interaction, see (26). To assess the model's performance we carried out tests for noncollinear spin structures of bcc Fe. We began by generating noncollinear training sets for $2 \times 2 \times 2$ supercells of a simple cubic description of bcc Fe containing 16 atoms with temperatures ranging from 0K to 1000K. To do this, we used the Uppsala atomic spin dynamics (UppASD) package [13, 14]. Once equilibrium was reached at each temperature, 50 spin structures were selected at random and divided into sets of 25 for training with the remaining 25 being used for testing.

A. Tests on DFT constrained calculations

To calculate the total energy of the non-collinear spin systems accurately, we performed constrained density functional theory calculations with the Vienna Ab-initio Simulation Package (VASP). The spin configurations were constrained so their orientations matched those of the training set output from UppASD and the perpendicular part of the internal effective field, about which the spins precess, was determined as the negative of the constraining field [32]. Exchange and correlation effects were described in the generalized gradient approximation as given by Perdew, Burke, and Ernzerhof [33]. An energy cut-off of 500 eV with energy converging to 10^{-6} eV was used. An equivalent $36 \times 36 \times 36$ k-point sampling for $1 \times 1 \times$ was used. The DFT energies of the noncollinear spin systems used for training were defined with respect to the corresponding collinear ferromagnetic system as

$$E_{\text{DFT}} = E_{\text{FM}}^{\text{nc}} - E_{\text{FM}}^{\text{c}}, \tag{37}$$

where $E_{\text{FM}}^{\text{nc}}$ and E_{FM}^{c} are the total energy for noncollinear and collinear systems, respectively. Because of the small size of the magnetocrystalline anisotropy energy (MAE) for cubic systems [34], spin orbit coupling was not included. Its effect will be studied at some later date for lower symmetry systems with larger MAEs [35, 36].

In the ML model, a cut-off radius of 7 Å was used to account for the exchange interaction between Fe atoms.

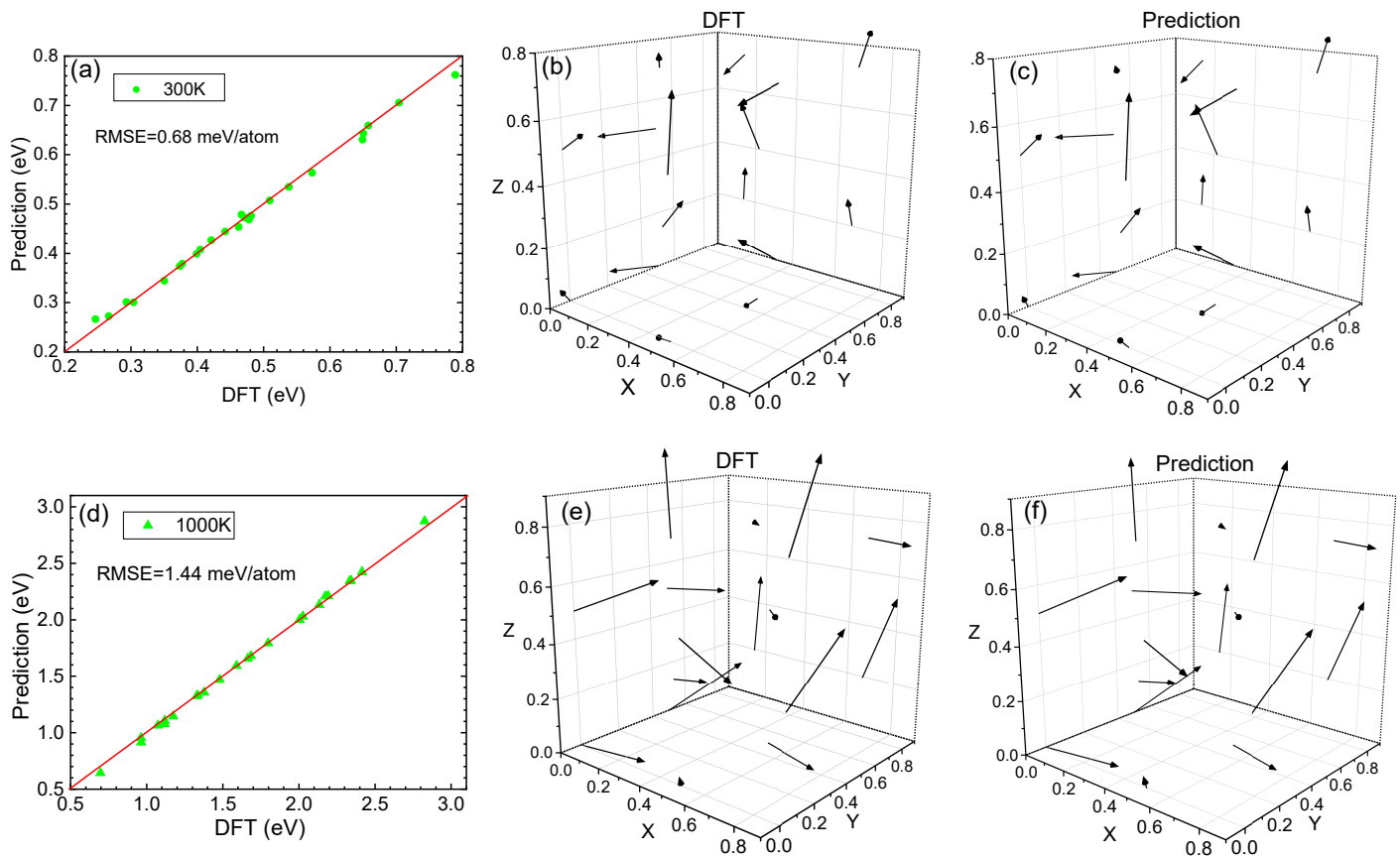


FIG. 2. Comparison of total DFT energies calculated for non-collinear configurations of 16 atom supercells of Fe with those predicted using the ML model at (a) 300K and (d) 1000K, respectively. All energies are given with respect to the energy of the corresponding collinear system and RMSE is the root mean square error. The ML exchange field model is trained with 25 different noncollinear spin configurations. (b,c) and (e,f) Comparison of the effective magnetic fields (arrows) on the Fe atoms from explicit DFT calculations (b) and (e) with the ML predictions (c) and (f) at 300K (b) and (c) and at 1000K (e) and (f), respectively. The unit of the effective magnetic field is eV/μ_B and is scaled by a factor of 4 for visualization purposes.

The maximum values of n and l for the spherical harmonics were set to 12 and 6, respectively. Fig. 2 compares total DFT energies and effective magnetic fields calculated for noncollinear configurations with the corresponding quantities predicted by the ML model at 300 K and 1000 K. The results demonstrate that the ML magnetic PES, trained with a very small set of 25 spin structures, accurately predicts the total energies and effective exchange fields of noncollinear spin structures. The root-mean-square error (RMSE) of the total energy is less than 1 meV/spin at 300 K, increasing to 1.44 meV/spin at 1000K. The larger RMSE at 1000 K compared to that at 300K suggests the need for a more extensive training set to represent the phase space of spin structures at higher temperatures more faithfully. To obtain the complete magnetic PES of bcc Fe may require training the model with sets that sample a larger part of the entire phase spaces ranging from 0K to the phase transition temperature.

The effective magnetic field shown in Fig. 2 is the transverse component of the total effective magnetic field

for each spin which generates the torque that describes the spin precession. This component is obtained using the expression

$$\mathbf{B}_{\perp}^i = -\frac{\partial E_i(\hat{\mathbf{e}}_i, \mathbf{r}_i)}{\partial \hat{\mathbf{e}}_i}. \quad (38)$$

One notable point is that the total energy learned by our model does not depend on the spin magnitude $|s_i|$, the \mathbf{B}_{\perp}^i can be obtained directly by the partial derivative of the total energy with respect to the spin unit vector $\hat{\mathbf{e}}_i$. This is confirmed by the results shown in the right-hand panels of Fig. 2. While \mathbf{B}_{\perp}^i gives rise to a torque on the spin, the longitudinal part of the effective field primarily governs the magnitude of the spin, which is not included in the present model; the noncollinear spin configurations for training and prediction only involve spin directions.

In principle, the exchange field which constrains the spin to the preferred direction in DFT calculations is equivalent to \mathbf{B}_{\perp}^i so we can compare the predicted \mathbf{B}_{\perp}^i and the constraining magnetic field obtained from DFT calculations. As seen in Fig. 2, the ML model accu-

rately predicts the perpendicular component of the effective magnetic field which can be leveraged in spin dynamics simulations. While the spin direction from the DFT and predictions align closely (maximum 5° difference), we observe that the magnitude of the effective exchange field from DFT calculations exceeds the prediction by a factor ranging from 1.0 to 1.2 on a few atomic sites, see Fig. 2 (e,f). This discrepancy can be attributed to the non-zero constraining penalty term in the constrained DFT calculations [32], where the spin direction approaches the preferred direction as the penalty term goes to zero. The constraining magnetic field obtained from constrained DFT calculations (as implemented in VASP) is given by

$$\mathbf{B}_{\text{Con}}^i = -\frac{\partial E_P}{\partial \mathbf{s}_i} = -\lambda_i(\hat{\mathbf{e}}_i - \hat{\mathbf{e}}_i^F) \quad (39)$$

in which E_P denotes the penalty energy, λ_i represents the parameter used in the constrained DFT calculations and $\hat{\mathbf{e}}_i$ and $\hat{\mathbf{e}}_i^F$ represent the unit spin direction and the preferred spin direction of atom i [32]. From (39), we can see that the constraining magnetic field obtained from DFT is either perpendicular to the spin direction or the preferred spin direction. Estimating the perpendicular exchange field using (38) generates an exchange field perpendicular to $\hat{\mathbf{e}}_i$. As a consequence, the magnitude and direction of the predicted exchange field may deviate from the DFT value but this can be improved as the penalty term converges to zero. However, this disparity does not compromise the accuracy of the effective magnetic field prediction with our ML model. It is worth noting that we train the ML model using spin configuration $\{\hat{\mathbf{e}}_i\}$ obtained from constrained DFT calculations, rather than the preferred spin configuration $\{\hat{\mathbf{e}}_i^F\}$.

A very useful feature of the MLFF is its portability allowing the model trained on small supercells to accurately predict the properties of significantly larger supercells. To assess the portability of our model, we employed the ML model trained with bcc Fe in a 16 atom supercell at 300K to predict the total energy of bcc Fe in $3 \times 3 \times 3$ cubic supercell containing 54 Fe atoms also at the same temperature. Because of the computational expense of constrained noncollinear calculations in larger supercells, only 12 samples were selected for testing. As demonstrated in Fig. 3, the trained model effectively predicts the total energy of the larger supercell, with the RMSE remaining consistent compared to that in the $2 \times 2 \times 2$ supercell.

B. Tests on Heisenberg Hamiltonian

The simplified Hamiltonian based on Heisenberg model can be constructed as

$$E = \sum_{i \neq j} J_{ij}(R) \mathbf{s}_i \cdot \mathbf{s}_j. \quad (40)$$

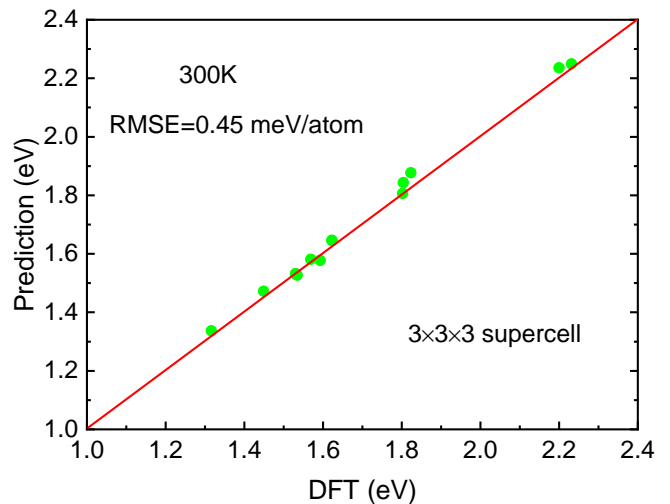


FIG. 3. Comparison of total DFT energies calculated for non-collinear configurations of 54 atom supercells of Fe with those predicted using the ML model. The ML model are trained with $2 \times 2 \times 2$ supercell of bcc Fe.

where only the exchange interaction is included and the exchange parameters $J_{ij}(R)$ were fitted from DFT calculations. 2550 random noncollinear spin configurations were produced in a $2 \times 2 \times 2$ supercell of bcc Fe, with the average angle between spins varying from 0 to π . Among these configurations, 50 were allocated for training the model, while the remaining 2500 were reserved for testing. The Heisenberg Hamiltonian was utilized to compute the total energy of each spin configuration. As depicted in Fig. 4 (a), the nearly perfect prediction achieved by the ML model, with just 50 training sets, underscores its exceptional performance. The error distribution, as shown in the inset, predominantly centers around 0 with an RMSE of 0.07 meV/atom. Notably, in this Heisenberg Hamiltonian, the magnetic moment remains fixed at $2.23 \mu_B$ and the exchange interaction parameter solely relies on the distance between two spins.

In a real system, the variations in magnetic moment and exchange interactions with temperature, particularly in noncollinear spin configurations, render accurate predictions challenging with a simplistic model that only considers spin directions. As illustrated in Fig. 7, the magnetic moment of bcc Fe shifts from $2.23 \mu_B$ in FM state to $1.60 \mu_B$ with antiparallel spins at the equilibrium lattice constant of GGA. According to the "adiabatic approximation" of spin, the magnitude of the moment should be slaved to the spin configurations. Our ML model that solely includes the spin direction should be enough to predict the total energy. However, to check the impact of the variation of the local magnetic moment on the performance of our model, we constructed a Heisenberg Hamiltonian with the magnetic moment of

spin i set by

$$M_i = 2.2 - \sum_{i \neq j}^j \frac{\arccos(\mathbf{e}_i \cdot \mathbf{e}_j)}{n\pi} \times 0.6, \quad (41)$$

in which n represents the total number of neighbours of spin i . As indicated in Fig. 4 (b), the spin configuration dependent magnetic moment elevates the RMSE of the prediction to 0.84 meV/atom, still remaining small compared to the total energy. As shown in Fig. 2, the RMSE increases at 1000 K compared to 300 K, attributed not only to the larger phase space at 1000K but also to the variation of the magnetic moment due to increased spin disorder at higher temperatures. The prediction accuracy can be enhanced with larger training sets. Although the changes in magnetic moment are not incorporated in our ML model, it proficiently predicts the total energy of the Heisenberg model. The energy scale (~ 4 -10 eV) of the Heisenberg model are much larger than that in DFT calculations, primarily because the angles between spins in the Heisenberg model are distributed in the range $[0, \pi]$, whereas the angles in DFT calculations obtained from Uppsala ASD simulations are much smaller ($\sim 0.4\pi$).

It is worth noting that the noncollinear spin systems in both Fig. 2 and Fig. 4 are situated at fixed atomic positions. In our ML model, the descriptor relies on both the spin direction and atomic coordinates. To evaluate the model's performance on systems with varying spin configurations and atomic distributions, we introduce a Gaussian distribution of lattice displacement in the non-collinear spin systems from their equilibrium positions. The Gaussian probability distribution is expressed as

$$P(\Delta r) = \frac{1}{\sqrt{2\pi}\sigma} \exp\left(-\frac{(\Delta r)^2}{2\sigma^2}\right), \quad (42)$$

where σ represents the broadening of the displacement and Δr denotes the displacement length. The Curie temperature of bcc Fe is around 1043K, corresponding to a thermal energy of 82 meV. To mimic the spin configuration and lattice displacement in actual systems, the average angle between spin at 1000 K can be estimated to 0.4π , considering the energy needed to flip the spin shown in Table I. As illustrated in Fig. 7, the lattice expands slightly with temperature, e.g. 1.5% at Curie temperature. Here we choose the σ to be 0.07 Å and 0.25 Å, which correspond to 1.2 % and 4.4 % of lattice expansion, respectively.

As proposed in [], the distance-dependent exchange interaction $J(r)$ can be parameterized using the double exchange interaction form

$$J(r) = \begin{cases} \frac{c}{r^3} e^{-r/r_0}, & \text{if } r \leq r_c \\ 0, & \text{otherwise.} \end{cases} \quad (43)$$

in which r denotes the distance between Fe atoms, and r_c represents the cutoff length of the exchange interaction. In the Heisenberg model, c and r_0 are set to be

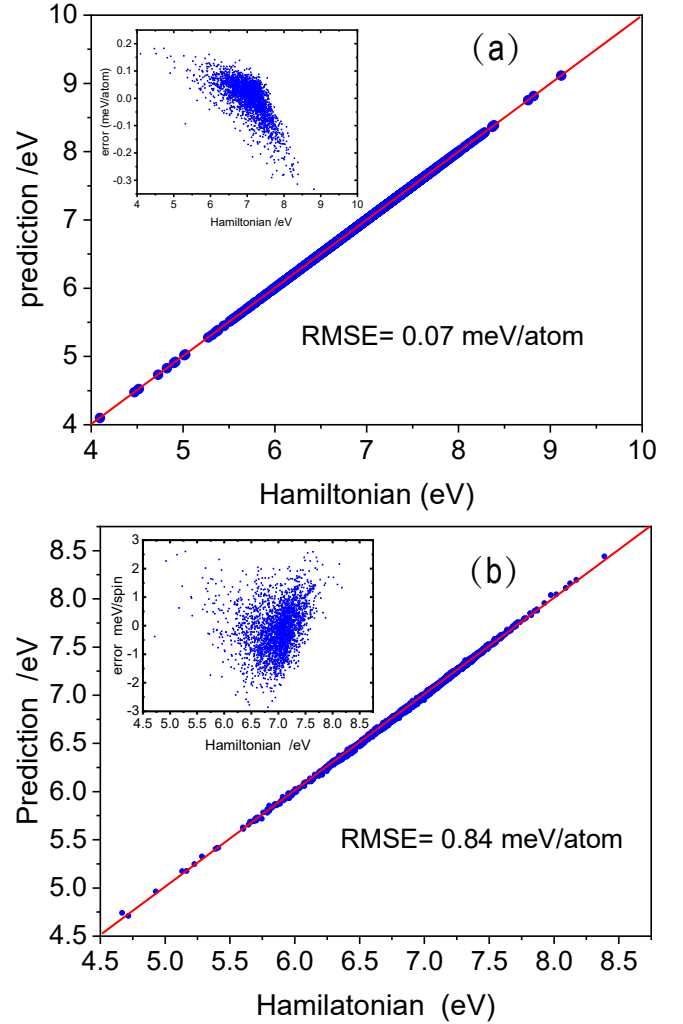


FIG. 4. The comparison between total energy from the prediction and Heisenberg Hamiltonian with (a) fixed magnetic moment and spin configuration dependent magnetic moment in $2 \times 2 \times 2$ supercell of bcc Fe. The inset shows the error distribution in the unit of meV/atom.

$0.94 \text{ eV}/\text{\AA}^3$ and 2.0 \AA by fitting the DFT calculations, respectively. Although it can not exactly reproduce the exchange interaction of bcc Fe, this model serves only to test the model's performance on the spin-lattice coupling. Because the exchange interaction between the nearest and second nearest neighbours contribute significantly to bcc Fe, r_c is set to 1.4 times the lattice constant.

Fig. 5 demonstrates the performance of the ML model on the spin-lattice coupling. The model can well predict the total energy for systems with diverse spin and atomic structures. The RMSE marginally increases as the atomic displacement broadens from 0.07 Å to 0.25 Å. Furthermore, it should be acknowledged that the atomic displacement is expected to influence the magnetization density and consequently the magnitude of the moment, as indicated in Appendix B. However, this is beyond the scope of this paper.

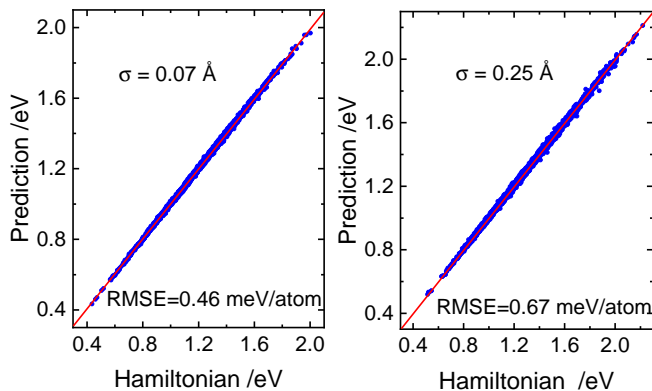


FIG. 5. The comparison between total energy of the prediction and Heisenberg Hamiltonian with atomic displacements in $2 \times 2 \times 2$ supercell of bcc Fe. The atomic displacements are sampled in Gaussian distribution with (a) $\sigma = 0.07 \text{ \AA}$ and (b) 0.25 \AA .

IV. DISCUSSION

In this paper, we introduced a novel descriptor for non-collinear spin systems within the GAP-SOAP framework. Under the "spin adiabatic approximation", the descriptor relies solely on the spin directions and the corresponding atomic coordinates where the spins are situated. By evaluating the smooth overlap of the spin directions in two local spin configurations, the similarity between them can be accurately assessed. The formulation of the descriptor and similarity kernel for both the exchange interaction and magnetic dipole-dipole interaction has been elucidated, and a descriptor incorporating a two-body term of the exchange interaction has been implemented and tested. The remarkable performance in predicting the total energy and internal effective magnetic field of non-collinear spin systems with a relative small training set underscores the robust capability of the proposed model.

A. ML model vs the magnetic cluster expansion

The equivalence between the GAP-SOAP power spectrum and the atomic cluster expansion with three-body term in spherical harmonics [37] suggests that the cluster expansion including spin and atomic coordinates will be analogous to the descriptor for spin and coordinates within the framework of GAP-SOAP. In the atomic cluster expansion, the angular momentum coupled to zero ($L=0$) signifies the rotation invariance. Recently, Matteo Rinaldi proposed a complete set for noncollinear spin systems based on the magnetic cluster expansion [38]. In comparison to their model, we have introduced an "adiabatic approximation" for the spin magnitude and spin direction, simplifying the model and enhancing its computational efficiency, while the training sets in atomic cluster expansion are in the order of 10^4 to achieve proper accuracy [38]. The estimated variation in the moment's

magnitude of bcc Fe, as the spin configurations transition from FM to AFM, is approximately 26 %, as deduced from Appendix B. At 1000K, the average spin angles is approximately 0.4π , obtained from spin dynamics simulations, suggesting that the variation of the magnetic moment below the Curie temperature of bcc Fe is restricted to roughly 10 %. As denoted in ??, the perpendicular component of the effective magnetic field relies solely on the spin unit vector rather than the spin magnitude. Consequently, the internal magnetic field can be accurately predicted without including the spin magnitude.

Our work have demonstrated that a two-body term of exchange interaction alone can sufficiently capture the exchange field. Another significant distinction lies in our incorporation of rotational invariance for various magnetic interactions. Instead of encompassing the two-spin, three-spin, and many-spin interaction term as in the atomic cluster expansion, we have constructed two-body, three-body, and many-body terms for different magnetic interactions, each possessing unique rotational symmetries. This approach makes our ML model more efficient and precise to include the magnetic interactions in interest.

B. ML model vs Spectral neighbor representation

ML models based on the spectral neighbor representation for noncollinear spin have been proposed [39]. This model introduces the rotational invariance of the neighbour vector field. However, the system is invariant under the rotation of the entire system and does not account for the rotational symmetries for different kinds of magnetic interactions. For instance, the exchange interaction should remain invariant under the rotation of s_i and s_j . Moreover, the vector spin on the rotation origin will destroy this kind of rotational invariance, although specific techniques can be applied to solve this issue [39].

Suzuki [40] extended the spectral neighbour representation to the GAP-SOAP framework, which is quite similar to our model. Their model does not rely on the rotation origin but the rotational invariance for different types of magnetic interactions are not specified in the model. They found that a higher-order partial spectrum (trispectrum) is necessary to accurately distinguish magnetic structures with different magnetic anisotropy. However, the trispectrum is equivalent to the five-body term descriptor for the magnetic dipole-dipole interaction in our model, which demands an extensive training set. By utilizing the spin adiabatic approximation and incorporating rotational invariance for specific magnetic interactions, such as exchange interaction, we have demonstrated that only a two-body term of exchange interaction in our model can accurately describe the total magnetic energy and internal effective magnetic field through training on DFT constrained calculations with a relative small training set.

V. CONCLUSION

In this paper, we have developed a highly accurate and efficient descriptor for noncollinear spin systems within the GAP-SOAP framework. The descriptors are designed with specific rotational invariant symmetries, tailored to different types of magnetic interactions. Leveraging the spin "adiabatic approximation" in the ML model has enhanced its efficiency, requiring only small training sets to achieve robust performance. Through constrained DFT calculations, we trained the ML model that only incorporates a simple two-body term of the exchange interaction with 25 different noncollinear spin configurations at each temperature. Despite the potential numerical error induced by the non-zero constraining penalty term in the DFT calculations, the ML model accurately forecasts the total energy and internal effective magnetic field with exceptional precision (around 1 meV/spin for the total energy and a maximum 5-degree difference for the magnetic field) relative to the DFT outcomes. In conclu-

sion, an efficient ML model for the noncollinear spin systems proposed in this paper can predict the total energy and effective magnetic field in the accuracy of DFT, at a significantly lower computational cost. Furthermore, this advancement paves the way for machine learning spin dynamics and a combination of ML spin dynamics and molecular dynamics can be expected, enabling investigation into various phenomena stemming from spin-lattice coupling effects, such as magneto-elastic effects, and magnon-phonon interactions.

ACKNOWLEDGMENTS

This work was financially supported by the "Nederlandse Organisatie voor Wetenschappelijk Onderzoek" (NWO) through the research programme of the former "Stichting voor Fundamenteel Onderzoek der Materie," (NWO-I, formerly FOM) and through the use of supercomputer facilities of NWO "Exacte Wetenschappen" (Physical Sciences). Y.G. thanks AHNU start-up grant for financial support.

Appendix A: Three body term for magnetic exchange like interaction

Three body term descriptor

$$\rho_i(r_1, r_2, \mathbf{e}_1, \mathbf{e}_2, \mathbf{e}_3) = \iint d\hat{\mathbf{r}}_1 d\hat{\mathbf{r}}_2 \sum_{j \neq k}^{N_a} f_{\text{cut}}(r_{ij}) g(\mathbf{r}_1 - \mathbf{r}_{ij}) g(\mathbf{r}_2 - \mathbf{r}_{ik}) g(\mathbf{e}_1 - \mathbf{e}_i) g(\mathbf{e}_2 - \mathbf{e}_j) g(\mathbf{e}_3 - \mathbf{e}_k) \quad (\text{A1})$$

The overlap S of the three-body term descriptor is

$$\begin{aligned} S(R) &= \iiint r_1^2 dr_1 r_2^2 dr_2 de_1 de_2 de_3 \rho(r_1, r_2, e_1, e_2, e_3) \rho'(r_1, r_2, Re_1, Re_2, Re_3) \\ &= \sum_{\substack{m, m_1, m_2 \\ m', m'_1, m'_2 \\ l, l_1, l_2}} C_{ll_1 l_2 m m_1 m_2}^* C'_{ll_1 l_2 m' m'_1 m'_2} D_{mm'}^l(R) D_{m_1 m'_1}^{l_1}(R) D_{m_2 m'_2}^{l_2}(R) \end{aligned} \quad (\text{A2})$$

The kernel for the three-body term descriptor

$$\begin{aligned} K(\rho, \rho') &= \int S(R) dR = \sum_{\substack{m, m_1, m_2 \\ m', m'_1, m'_2 \\ l, l_1, l_2}} C_{ll_1 l_2 m m_1 m_2}^* C'_{ll_1 l_2 m' m'_1 m'_2} \int D_{mm'}^l(R) D_{m_1 m'_1}^{l_1}(R) D_{m_2 m'_2}^{l_2}(R) dR \\ &= \sum_{\substack{m, m_1, m_2 \\ m', m'_1, m'_2 \\ l, l_1, l_2}} C_{ll_1 l_2 m m_1 m_2}^* C'_{ll_1 l_2 m' m'_1 m'_2} (-1)^{m-m'} \int D_{-m, -m'}^l(R)^* D_{m_1 m'_1}^{l_1}(R) D_{m_2 m'_2}^{l_2}(R) dR \\ &= \sum_{\substack{m, m_1, m_2 \\ m', m'_1, m'_2 \\ l, l_1, l_2}} C_{ll_1 l_2 m m_1 m_2}^* C'_{ll_1 l_2 m' m'_1 m'_2} \frac{8\pi^2 (-1)^{m+m'}}{2l+1} \langle l, -m | l_1 m_1; l_2 m_2 \rangle \times \langle l, -m' | l_1 m'_1; l_2 m'_2 \rangle \end{aligned} \quad (\text{A3})$$

The atomic densities are written as

$$\begin{aligned} \rho_i(r_1) &= \frac{1}{\sqrt{4\pi}} \sum_{n=1}^{N_R} C_n^i \chi_{nl}(r_1) \quad ; \quad \rho_i(r_2) = \frac{1}{\sqrt{4\pi}} \sum_{n=1}^{N_R} C_n^i \chi_{nl}(r_2) \\ C_{ll_1l_2, m_1m_2}^i &= \sum_j^{N_a} \left(\frac{4}{I_0(\frac{1}{\sigma^2})} \right)^3 j_l \left(\frac{1}{\sigma^2} \right) j_{l_1} \left(\frac{1}{\sigma^2} \right) j_{l_2} \left(\frac{1}{\sigma^2} \right) Y_{lm_1+m_2}(\hat{\mathbf{e}}_i) Y_{l_1m_1}^*(\hat{\mathbf{e}}_j) Y_{l_2m_2}^*(\hat{\mathbf{e}}_k) \\ &\quad \times \sqrt{\frac{8\pi^2}{2l+1}} \langle l, m_1 + m_2 | l_1 m_1; l_2 m_2 \rangle \end{aligned} \quad (\text{A4})$$

Finally, the coefficients for the kernel become

$$\begin{aligned} C_{nn' ll_1l_2, m_1m_2}^i &= \frac{1}{4\pi} C_{n'00}^i C_{n00}^i \sum_{j,k}^{N_a} \left(\frac{4}{I_0(\frac{1}{\sigma^2})} \right)^3 j_l \left(\frac{1}{\sigma^2} \right) j_{l_1} \left(\frac{1}{\sigma^2} \right) j_{l_2} \left(\frac{1}{\sigma^2} \right) Y_{lm_1+m_2}(\hat{\mathbf{e}}_i) Y_{l_1m_1}^*(\hat{\mathbf{e}}_j) Y_{l_2m_2}^*(\hat{\mathbf{e}}_k) \\ &\quad \times \sqrt{\frac{8\pi^2}{2l+1}} \langle l, m_1 + m_2 | l_1 m_1; l_2 m_2 \rangle \end{aligned} \quad (\text{A5})$$

The kernel

$$K(\rho_i, \rho'_i) = \sum_{nn' ll_1l_2, m_1m_2} C_{nn' ll_1l_2, m_1m_2}^{i*} C_{nn' ll_1l_2, m'_1m'_2}^i \quad (\text{A6})$$

Another kind of "three body term" with a bit more strict constraints on the relative atomic position can be defined by the independent rotation invariant symmetry of (r_{ij}, r_{ik}) and (e_i, e_j, e_k) , which lies in-between the three body terms of magnetic dipole-dipole interaction and exchange interaction. This three body term should be more efficient in describing the non-collinear effect which originates from the interaction between neighbouring spins.

The overlap of the new "three body term" descriptor

$$\begin{aligned} S(R_1, R_2) &= \iiint r_1^2 dr_1 r_2^2 dr_2 d\hat{\mathbf{e}}_1 d\hat{\mathbf{e}}_2 d\hat{\mathbf{e}}_3 \rho(r_1, r_2, \hat{\mathbf{e}}_1, \hat{\mathbf{e}}_2, \hat{\mathbf{e}}_3) \rho'(R_1 r_1, R_1 r_2, R_2 \hat{\mathbf{e}}_1, R_2 \hat{\mathbf{e}}_2, R_2 \hat{\mathbf{e}}_3) \\ &= \sum_{\substack{m, m_1, m_2 \\ m', m'_1, m'_2 \\ l, l_1, l_2}} C_{LL_1 MM_1}^* C'_{LL_1 M' M'_1} C_{ll_1 l_2 m_1 m_2 m_3}^* C'_{ll_1 l_2 m'_1 m'_2 m'_3} C_{MM'}^L(R_1) D_{M_1 M'_1}^{L_1}(R_1) D_{mm'}^l(R_2) D_{m_1 m'_1}^{l_1}(R_2) D_{m_2 m'_2}^{l_2}(R_2) \end{aligned}$$

The kernel for the three-body term descriptor

$$\begin{aligned} K(\rho, \rho') &= \iint S(R_1, R_2) dR_1 dR_2 \\ &= \sum_{\substack{m, m_1, m_2 \\ m', m'_1, m'_2 \\ l, l_1, l_2}} C_{LL_1 MM_1}^* C'_{LL_1 M' M'_1} C_{ll_1 l_2 m m_1 m_2}^* C'_{ll_1 l_2 m' m'_1 m'_2} \\ &\quad \times \int D_{MM'}^L(R_1) D_{M_1 M'_1}^{L_1}(R_1) dR_1 \int D_{mm'}^l(R) D_{m_1 m'_1}^{l_1}(R) D_{m_2 m'_2}^{l_2}(R) dR_2 \\ &= \sum_{\substack{m_1, m_2 \\ m'_1, m'_2 \\ l_1, l_2}} C_{l_1 l_2 m_1 m_2}^* C'_{l_1 l_2 m'_1 m'_2} (-1)^{m_1 - m'_1} \int D_{-m_1, -m'_1}^{l_1}(R)^* (R) D_{m_2 m'_2}^{l_2}(R) dR \\ &\quad \times \sum_{\substack{m, m_1, m_2 \\ m', m'_1, m'_2 \\ l, l_1, l_2}} C_{ll_1 l_2 m m_1 m_2}^* C'_{ll_1 l_2 m' m'_1 m'_2} (-1)^{m - m'} \int D_{-m, -m'}^l(R)^* (R) D_{m_1 m'_1}^{l_1}(R) D_{m_2 m'_2}^{l_2}(R) dR \\ &= \sum_{M_1, M'_1, L} \frac{8\pi^2 (-1)^{M_1 + M'_1}}{2L + 1} C_{LM_1, -M_1}^* C'_{LM'_1, -M'_1} \sum_{\substack{m, m_1, m_2 \\ m', m'_1, m'_2 \\ l, l_1, l_2}} C_{ll_1 l_2 m m_1 m_2}^* C'_{ll_1 l_2 m' m'_1 m'_2} \\ &\quad \times \frac{8\pi^2 (-1)^{m + m'}}{2l + 1} \langle l, -m | l_1 m_1; l_2 m_2 \rangle \langle l, -m' | l_1 m'_1; l_2 m'_2 \rangle \end{aligned} \quad (\text{A7})$$

$$\rho_i(r_1) = \frac{1}{\sqrt{4\pi}} \sum_{n=1}^{N_R} C_n^i \chi_{nl}(r_1) \quad ; \quad \rho_i(r_2) = \frac{1}{\sqrt{4\pi}} \sum_{n=1}^{N_R} C_n^i \chi_{nl}(r_2)$$

$$C_{ll_1l_2, m_1m_2}^i = \sum_j^{N_a} \left(\frac{4}{I_0\left(\frac{1}{\sigma^2}\right)} \right)^3 j_l\left(\frac{1}{\sigma^2}\right) j_{l_1}\left(\frac{1}{\sigma^2}\right) j_{l_2}\left(\frac{1}{\sigma^2}\right) Y_{lm_1+m_2}(\hat{\mathbf{e}}_i) Y_{l_1m_1}^*(\hat{\mathbf{e}}_j) Y_{l_2m_2}^*(\hat{\mathbf{e}}_k) \quad (\text{A8})$$

$$\times \sqrt{\frac{8\pi^2}{2l+1}} \langle l, m_1 + m_2 | l_1 m_1; l_2 m_2 \rangle$$

Finally, the coefficients for the kernel become

$$C_{nn' ll_1 l_2, m_1 m_2}^i = \frac{1}{4\pi} C_{n00}^i C_{n'00}^i \sum_{j,k}^{N_a} \left(\frac{4}{I_0\left(\frac{1}{\sigma^2}\right)} \right)^3 j_l\left(\frac{1}{\sigma^2}\right) j_{l_1}\left(\frac{1}{\sigma^2}\right) j_{l_2}\left(\frac{1}{\sigma^2}\right) Y_{lm_1+m_2}(\hat{\mathbf{e}}_i) Y_{l_1m_1}^*(\hat{\mathbf{e}}_j) Y_{l_2m_2}^*(\hat{\mathbf{e}}_k) \quad (\text{A9})$$

$$\times \sqrt{\frac{8\pi^2}{2l+1}} \langle l, m_1 + m_2 | l_1 m_1; l_2 m_2 \rangle$$

where the kernel

$$K(\rho_i, \rho'_i) = \sum_{nn' ll_1 l_2, m_1 m_2} C_{nn' ll_1 l_2, m_1 m_2}^{i*} C_{nn' ll_1 l_2, m_1' m_2'}^i \quad (\text{A10})$$

Appendix B: The lattice constant dependence of total energy and local magnetic moment of bcc Fe

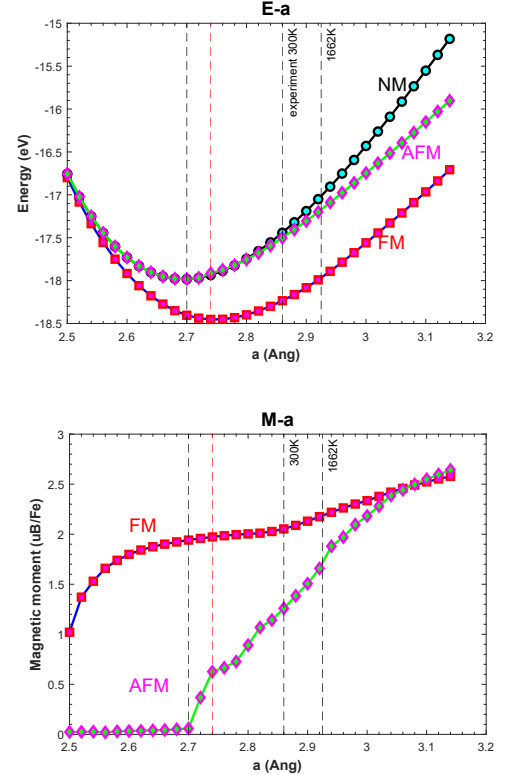


FIG. 6. The total energy and local magnetic moment of bcc Fe as a function of lattice constant for FM, AFM and NM states calculated with LDA.

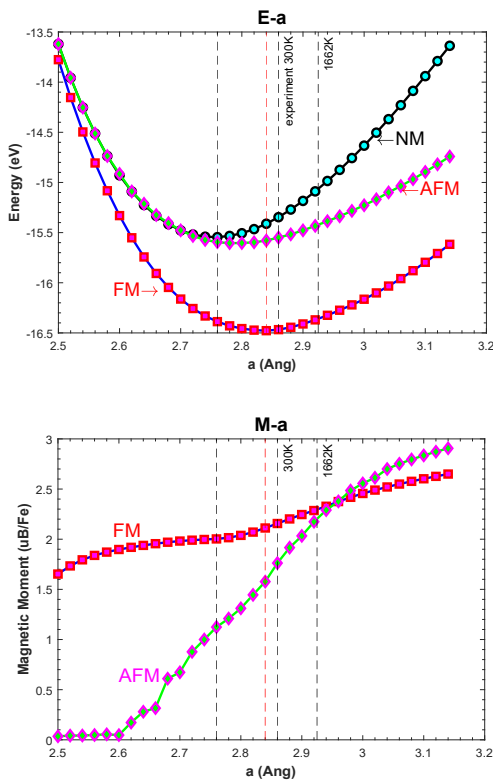


FIG. 7. The total energy and local magnetic moment of bcc Fe as a function of lattice constant for FM, AFM and NM states calculated with GGA.

-
- [1] R. Car and M. Parrinello, Unified approach for molecular dynamics and density-functional theory, *Phys. Rev. Lett.* **55**, 2471 (1985).
- [2] J. Behler and M. Parrinello, Generalized neural-network representation of high-dimensional potential-energy surfaces, *Phys. Rev. Lett.* **98**, 146401 (2007).
- [3] P. Hohenberg and W. Kohn, Inhomogeneous electron gas, *Phys. Rev.* **136**, B864 (1964).
- [4] W. Kohn and L. J. Sham, Self-consistent equations including exchange and correlation effects, *Phys. Rev.* **140**, A1133 (1965).
- [5] A. N. Other and S. W. Els, We need a reference here, *Adv. Phys.* **27**, 799 (1978).
- [6] J. Behler, Perspective: Machine learning potentials for atomistic simulations, *J. Chem. Phys.* **145**, 170901 (2016).
- [7] A. P. Bartók, M. C. Payne, R. Kondor, and G. Csányi, Gaussian Approximation Potentials: The Accuracy of Quantum Mechanics, without the Electrons, *Phys. Rev. Lett.* **104**, 136403 (2010).
- [8] R. Jinnouchi, F. Karsai, and G. Kresse, On-the-fly machine learning force field generation: Application to melting points, *Phys. Rev. B* **100**, 014105 (2019).
- [9] A. P. Bartók, R. Kondor, and G. Csányi, On representing chemical environments, *Phys. Rev. B* **87**, 184115 (2013).
- [10] R. Jinnouchi, J. Lahnsteiner, F. Karsai, G. Kresse, and M. Bokdam, Phase Transitions of Hybrid Perovskites Simulated by Machine-Learning Force Fields Trained on the Fly with Bayesian Inference, *Phys. Rev. Lett.* **122**, 225701 (2019).
- [11] J. Miltat, G. Albuquerque, and A. Thiaville, An Introduction to Micromagnetics in the Dynamic Regime (Springer, Berlin, 2002) Chap. 1, pp. 1–34.
- [12] Y. Tserkovnyak, A. Brataas, G. E. W. Bauer, and B. I. Halperin, Nonlocal magnetization dynamics in ferromagnetic nanostructures, *Rev. Mod. Phys.* **77**, 1375 (2005).
- [13] B. Skubic, J. Hellsvik, L. Nordström, and O. Eriksson, A method for atomistic spin dynamics simulations: implementation and examples, *J. Phys.: Condens. Matter* **20**, 315203 (2008).
- [14] O. Eriksson, A. Bergman, L. Bergqvist, and J. Hellsvik, *Atomistic Spin Dynamics: Foundations and Applications* (Oxford University Press, Oxford, 2017).
- [15] A. P. Bartók and G. Csányi, Gaussian approximation potentials: A brief tutorial introduction, *International Journal of Quantum Chemistry* **115**, 1051 (2015).
- [16] M. Heine, O. Hellman, and D. Broido, Temperature-dependent renormalization of magnetic interactions by thermal, magnetic, and lattice disorder from first principles, *Phys. Rev. B* **103**, 184409 (2021).
- [17] M. Pajda, J. Kudrnovský, I. Turek, V. Drchal, and P. Bruno, Ab initio calculations of exchange interactions, spin-wave stiffness constants, and Curie temperatures of Fe, Co, and Ni, *Phys. Rev. B* **64**, 174402 (2001).

- [18] M. Born and R. J. Oppenheimer, Zur Quantentheorie der Molekeln (On the Quantum Theory of Molecules), *Annalen der Physik* **84**, 457 (1927).
- [19] V. P. Antropov, M. I. Katsnelson, M. van Schilfhaarde, and B. N. Harmon, *Ab Initio* spin dynamics in magnets, *Phys. Rev. Lett.* **75**, 729 (1995); V. P. Antropov, M. I. Katsnelson, B. N. Harmon, M. van Schilfhaarde, and D. Kusnezov, Spin dynamics in magnets: Equation of motion and finite temperature effects, *Phys. Rev. B* **54**, 1019 (1996).
- [20] R. M. White, *Quantum theory of magnetism*, 2nd ed., edited by M. Carona, P. Fulde, K. von Klitzing, and H.-J. Queisser, Springer Series in Solid-State Sciences, Vol. 32 (Springer, Berlin, 1983).
- [21] D. M. Paige, B. Szpunar, and B. K. Tanner, The magneto-crystalline anisotropy of cobalt, *J. Magn. Magn. Mater.* **44**, 239 (1984).
- [22] P. Escudier, L'anisotropie de l'aimantation: un paramètre important de l'étude de l'anisotropie magnétocristalline (magnetization anisotropy - important parameter for study of magnetocrystalline anisotropy) (1975) pp. 125–173.
- [23] G. Chen, J. Zhu, A. Quesada, J. Li, A. T. N'Diaye, Y. Huo, T. P. Ma, Y. Chen, H. Y. Kwon, C. Won, Z. Q. Qiu, A. K. Schmid, and Y. Z. Wu, Novel chiral magnetic domain wall structure in Fe/Ni/Cu (001) films, *Phys. Rev. Lett.* **110**, 177204 (2013).
- [24] H. Yang, G. Chen, A. A. C. Cotta, A. T. N'Diaye, S. A. Nikolaev, E. A. Soares, W. A. A. Macedo, K. Liu, A. K. Schmid, A. Fert, and M. Chshiev, Significant Dzyaloshinskii-Moriya interaction at graphene-ferromagnet interfaces due to the Rashba effect, *Nat. Mater.* **17**, 605 (2018).
- [25] G. Chen, T. Ma, A. T. N'Diaye, H. Kwon, C. Won, Y. Wu, and A. K. Schmid, Tailoring the chirality of magnetic domain walls by interface engineering, *Nat. Commun.* **4**, 2671 (2013).
- [26] R. Kikuchi, A theory of cooperative phenomena, *Phys. Rev.* **81**, 988 (1951).
- [27] S. N. Pozdnyakov, M. J. Willatt, A. P. Bartók, C. Ortner, G. Csányi, and M. Ceriotti, Incompleteness of Atomic Structure Representations, *Phys. Rev. Lett.* **125**, 166001 (2020).
- [28] K. Kaufmann and W. Baumeister, Single-centre expansion of Gaussian basis functions and the angular decomposition of their overlap integrals, *J. Phys. B: Atomic, Molecular and Optical Physics* **22**, 1 (1989).
- [29] (), In the QUIP code from Cambridge University, the radial parts are expanded in a set of equally spaced Gaussian functions while in the VASP ML package the radial basis functions are normalised spherical Bessel functions. The Gaussian basis functions need to be orthogonalised. The normalised spherical Bessel functions are mutually orthogonal.
- [30] (), The Born-Oppenheimer approximation makes use of the different time scales of electronic and nuclear motion determined by the electron and nuclear masses to integrate out the electronic degrees of freedom and calculate the PES that determines nuclear motion [18]. Because there is no moment of inertia associated with the electron spin, we must use the characteristic frequencies of different spin interactions to establish an adiabatic approximation [19].
- [31] E. P. Wigner, Group theory and its application to the quantum mechanics of atomic spectra, in *Group Theory and its application to the quantum mechanics of atomic spectra* (Academic Press, 1959).
- [32] P.-W. Ma and S. L. Dudarev, Constrained density functional for noncollinear magnetism, *Phys. Rev. B* **91**, 054420 (2015).
- [33] J. P. Perdew, K. Burke, and M. Ernzerhof, Generalized gradient approximation made simple, *Phys. Rev. Lett.* **77**, 3865 (1996).
- [34] G. H. O. Daalderop, P. J. Kelly, and M. F. H. Schuurmans, First-principles calculation of the magnetocrystalline anisotropy energy of iron, cobalt and nickel, *Phys. Rev. B* **41**, 11919 (1990).
- [35] G. H. O. Daalderop, P. J. Kelly, and F. J. A. den Broeder, Prediction and confirmation of perpendicular magnetic anisotropy in Co/Ni multilayers, *Phys. Rev. Lett.* **68**, 682 (1992).
- [36] G. H. O. Daalderop, P. J. Kelly, and M. F. H. Schuurmans, Magnetic anisotropy of a free-standing Co monolayer and of multilayers which contain Co monolayers, *Phys. Rev. B* **50**, 9989 (1994).
- [37] R. Drautz, Atomic cluster expansion for accurate and transferable interatomic potentials, *Phys. Rev. B* **99**, 014104 (2019).
- [38] M. Rinaldi, M. Mrovec, A. Bochkarev, Y. Lyso-gorskiy, and R. Drautz, Non-collinear magnetic atomic cluster expansion for iron, arXiv:2305.15137 10.48550/arXiv.2305.15137 (2023).
- [39] M. Domina, M. Cobelli, and S. Sanvito, Spectral neighbor representation for vector fields: Machine learning potentials including spin, *Phys. Rev. B* **105**, 214439 (2022).
- [40] M.-T. Suzuki, T. Nomoto, E. V. Morooka, Y. Yanagi, and H. Kusunose, High-performance descriptor for magnetic materials: Accurate discrimination of magnetic structure, *Phys. Rev. B* **108**, 014403 (2023).